Phase-Field Simulation of Fusion Interface Events during Solidification of Dissimilar Welds: Effect of Composition Inhomogeneity

SUBHRADEEP CHATTERJEE, T.A. ABINANDANAN, and KAMANIO CHATTOPADHYAY

We investigate the events near the fusion interfaces of dissimilar welds using a phase-field model developed for single-phase solidification of binary alloys. The parameters used here correspond to the dissimilar welding of a Ni/Cu couple. The events at the Ni and the Cu interface are very different, which illustrate the importance of the phase diagram through the slope of the liquidus curves. In the Ni side, where the liquidus temperature decreases with increasing alloying, solutal melting of the base metal takes place; the resolidification, with continuously increasing solid composition, is very sluggish until the interface encounters a homogeneous melt composition. The growth difficulty of the base metal increases with increasing initial melt composition, which is equivalent to a steeper slope of the liquidus curve. In the Cu side, the initial conditions result in a deeply undercooled melt and contributions from both constrained and unconstrained modes of growth are observed. The simulations bring out the possibility of nucleation of a concentrated solid phase from the melt, and a secondary melting of the substrate due to the associated recalescence event. The results for the Ni and Cu interfaces can be used to understand more complex dissimilar weld interfaces involving multiphase solidification.

DOI: 10.1007/s11661-007-9340-1
© The Minerals, Metals & Materials Society and ASM International 2007

I. INTRODUCTION

EVER since Metzger *et al.*'s substantial initial work on welding of dissimilar metal combinations,[1] a considerable amount of effort has gone into determining the weldability of specific dissimilar combinations (for example, the overviews by Sun and co-workers[2,3] summarize the progress made until the middle of the last decade). During recent years, computer simulations and experiments have helped us gain a better understanding of the fluid flow effects and development of the macroscopic weld pool geometry in dissimilar welds.[4–7] Studies have also been undertaken to elucidate the underlying mechanisms of microstructure formation in these welds in terms of fundamentals of solidification theory.[8–11] In this latter set of experiments, regions close to the fusion interfaces revealed microstructures that were remarkably different from the ones observed during welding of similar metals, and in this article, we seek to address some of the issues related to this aspect of dissimilar welding.

Nelson *et al.*,[8] while studying welding of different grades of steel in contact with a monel (Ni-rich Ni-Cu alloy) filler alloy melt, reported that when the primary solidifying phase had a crystal structure different from the base metal, epitaxial growth of the substrate (commonly found in welds between similar metals) was replaced by a chill zonelike microstructure. This microstructure consisted of numerous small grains, which nucleated heterogeneously on the substrate grains at the fusion interface. In contrast, they observed epitaxial growth when the composition change was not accompanied by a corresponding change in the crystal structure, implying a dominant role of the crystal structure of the primary phase over that of a difference only in composition.

However, the results of Phanikumar *et al.*[9] for laser welding of Cu and Ni, which form an isomorphous system with fcc structure, indicate that the composition gradient can affect interface microstructure even when the solidifying phase has the same crystal structure. They noted that while the Ni interface did exhibit epitaxy, the Cu interface was irregular and the fusion line was clearly separated from the alloyed weldment by an unmixed zone. In a later experiment on the immiscible Fe/Cu system, Phanikumar *et al.* also observed[10] the formation of Fe-rich bands at the Cu interface, which they attributed to a phase separation reaction in the liquid followed by peritectic solidification. For a closely related system, namely, the welding of stainless steel to copper, Magnabosco *et al.*[12] noted the absence of epitaxy at the fusion interfaces. During laser welding of a Ti/Ni couple, the present authors reported[11]

SUBHRADEEP CHATTERJEE, Research Associate, T.A. ABINANDANAN, Associate Professor, and KAMANIO CHATTOPADHYAY, Professor, are with the Department of Materials Engineering, Indian Institute of Science, Bangalore 560012, India. Contact e-mail: kamanio@materials.iisc.ernet.in

This article is based on a presentation given in the symposium entitled "Materials Behavior: Far from Equilibrium" as part of the Golden Jubilee Celebration of Bhabha Atomic Research Centre, which occurred December 15–16, 2006 in Mumbai, India.

Article published online October 30, 2007

dendritic growth of an intermediate phase (Ti_2Ni) directed *toward* the base metal near the Ti interface.

All of these examples of diverse microstructures highlight a qualitative shift from the conventional welding in terms of new phenomena that can occur at the fusion interfaces. These phenomena take place as a result of the intricate coupling between the heat transfer, on one hand, and the thermodynamics and kinetics of the system on the other. The phase-field approach has been shown to be an effective modeling technique, which captures this coupling in a very natural manner;[13] we have undertaken a computational study using this model to explore near-interface events during solidification of dissimilar welds. As a first step toward achieving the more general goal, here, we analyze the consequences of an abrupt jump in composition that exists near the fusion interfaces of dissimilar welds.

II. MODEL AND SIMULATION PARAMETERS

Since we are interested in modeling phase transformations in a highly nonisothermal environment, an entropy functional based approach becomes the natural choice.[14] This model, initially developed for pure metals by Wang *et al.*,[15] was later extended for binary alloys by Warren and Boettinger.[16] We describe here the salient features of the fully nonisothermal model for binary alloys given by Loginova *et al.*[17]

In this model, a phase-field variable (ϕ) distinguishes between liquid ($\phi = 1$) and solid ($\phi = 0$) regions, and it varies smoothly between these two values across the solid-liquid interface. The thermodynamics of the system is described by writing the total entropy of the system (S) as a functional of the phase field and its gradient:

$$S = \int_{\Omega} [s(\phi, c, e) - \frac{\epsilon^2}{2} |\nabla\phi|^2] d\Omega \qquad [1]$$

Here, s is the local entropy density, which is a function of the phase-field ϕ, composition c (mole fraction of solute B in a binary A-B alloy), and internal energy density e, which is postulated to be the composition averaged value of the energy densities of the individual constituents: $e = (1-c)e^A + ce^B$. The e^i's ($i = A, B$) can be expressed as follows: $e^i = e^i_S(T^i_m) + C^i_p(T - T^i_m) + p(\phi)L^i$, where L, C_p, and T_m are the latent heat of fusion, specific heat, and melting point of the pure constituents, respectively. The term $p(\phi)$ is a smooth interpolating function between 0 and 1 satisfying the conditions $p(0) = 0$ and $p(1) = 1$. The parameter ϵ^2 is gradient entropy constant related to the solid-liquid interfacial energy, and Ω represents the volume of the system.

The evolution equation for ϕ, which is a nonconserved parameter, can be derived by assuming relaxational dynamics, which guarantees positive entropy production.[15] Equations for composition and temperature (T) are obtained through conservation laws for mass and energy, respectively. Details of the derivations are available in References 15 through 17; here, we write only the final forms of the equations in one-dimension, noting that an ideal solution approximation has been used for the mixing of pure components A and B:

$$\dot{\phi} = M_\phi \left[\epsilon^2 \frac{\partial^2 \phi}{\partial x^2} - \{(1-c)H^A + cH^B\} \right] \qquad [2]$$

$$\dot{c} = \frac{\partial}{\partial x} D \left[\frac{\partial c}{\partial x} + \frac{v_m}{R} c(1-c)(H^B - H^A) \frac{\partial \phi}{\partial x} \right] \qquad [3]$$

$$\bar{C}_p \dot{T} = \frac{\partial}{\partial x} \left(\bar{K} \frac{\partial T}{\partial x} \right) - 30 g(\phi) \bar{L} \dot{\phi} \qquad [4]$$

Here, a dot over a quantity denotes its partial derivative with respect to time t, and x is the spatial variable. The term M_ϕ is a parameter related to interface mobility, and $\bar{K}$ is the thermal conductivity; these, along with $\bar{C}p$ and $\bar{L}$, are the composition averaged values of the corresponding pure component properties. The term v_m is the molar volume, R is the gas constant, and $g(\phi) = \phi^2(1-\phi)^2$ is the standard double well potential. The H^i's are given by

$$H^i(\phi, T) = W^i \frac{\partial g}{\partial \phi} + 30 g(\phi) L^i \left(\frac{1}{T} - \frac{1}{T^i_m} \right) \quad i = A, B \qquad [5]$$

where W is the height of the double well potential. For solute diffusion, the expression $D = D_S + p(\phi)(D_L - D_S)$ has been used, where D_S and D_L are classical diffusivities in solid and liquid, respectively. Other model parameters, namely, ϵ^2, M^i, and W, are obtained by performing a sharp interface asymptotic analysis,[16] which provides their relationship with interfacial energy σ, interface thickness δ, and interface attachment coefficient μ. The last quantity is defined by the relation

$$V = \mu^i (T^i_M - T_{\text{int}}) \qquad [6]$$

where V is the growth velocity, T_{int} is the interface temperature, and the quantity inside the parentheses is the "kinetic undercooling." The material properties (and model parameters determined from them) are listed in Table I; they correspond to the binary Ni-Cu system, and henceforth all references to the simulations will be made with respect to this system.

To mimic the conditions near the fusion interfaces during dissimilar welding, we have constructed a system with the initial and boundary conditions as depicted in Figure 1; two separate sets of simulations are performed for fusion interfaces in Ni and Cu, respectively. Simulations are started with pure solid Ni or Cu being kept in contact with an alloy melts of composition c_0; we use $c_0 = 0.25$ and $c_0 = 0.75$ for the Ni- and Cu-interface simulations, respectively. A positive temperature gradient (G) of 10^5 K/m is imposed initially in such a way that the solid-liquid interface temperature is at the melting point of the pure solid. Heat extraction through the cooler substrate during welding is introduced here through a negative heat flux condition at the left wall; the right wall is thermally insulated. We have chosen the

Table I. Model Parameters and Material Properties

Property/Parameter	Ni	Cu
T_m (K)	1728	1358
L (J/m^3)	2350×10^6	1728×10^6
σ (J/m^2)	0.37	0.29
D_L (m^2/s)	10^{-9}	10^{-9}
D_S (m^2/s)	10^{-13}	10^{-13}
C_p (J/(m^3 K))	5.42×10^6	3.96×10^6
K (J/(smK))	84	200
v_m (m^3/mole)	7.42×10^{-6}	7.42×10^{-6}
μ (m/(Ks))	3.3×10^{-3}	3.9×10^{-3}
δ (m)	4.9×10^{-9}	4.9×10^{-9}
W (J/(m^3 K))	9.27×10^3	9.245×10^3
M (m^3 K/(Js))	10.085	10.01
ϵ^2 (J/(mK))	8.9×10^{-11}	8.9×10^{-11}

Based on Data from References 16 and 17.

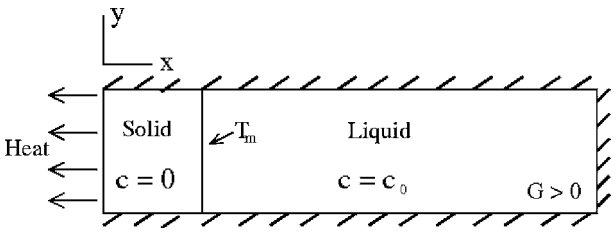

Fig. 1—Schematic representation of the computational setup. Refer to text for details.

magnitude of the flux $\dot{q}$ ($= -10^8$ J/m^{2}s) at the left wall to approximately correspond to the order of that obtained using Fourier's law of heat conduction, $\dot{q} = -K(dT/dx)$, with typical values being used for K and dT/dx. The system is closed with regard to composition, and we employ a symmetry boundary condition for the phase-field variable at both ends.

The governing equations are solved numerically using the finite difference discretization and implicit time integration scheme. All of the simulations use a uniform grid of spacing 25 nm; an upper bound for the value of the time-step is arrived at by the stability criterion of explicit Euler integration.[16] We present here the results of our one-dimensional simulations for a 500 μm long computational domain.

III. RESULTS

A. *Ni Interface*

Figures 2(a) through (c) describe the evolution of the field variables (ϕ, c, and T, respectively) at the Ni interface. For the phase-field and composition profiles, a small part of the domain where the only significant variation in these profiles takes place is shown; the global temperature profile in Figure 2(c) has this region zoomed in as an inset. As we can observe from the phase-field profile at time $t = 0.25$ ms in Figure 2(a), the pure Ni solid, which is initially in contact with a

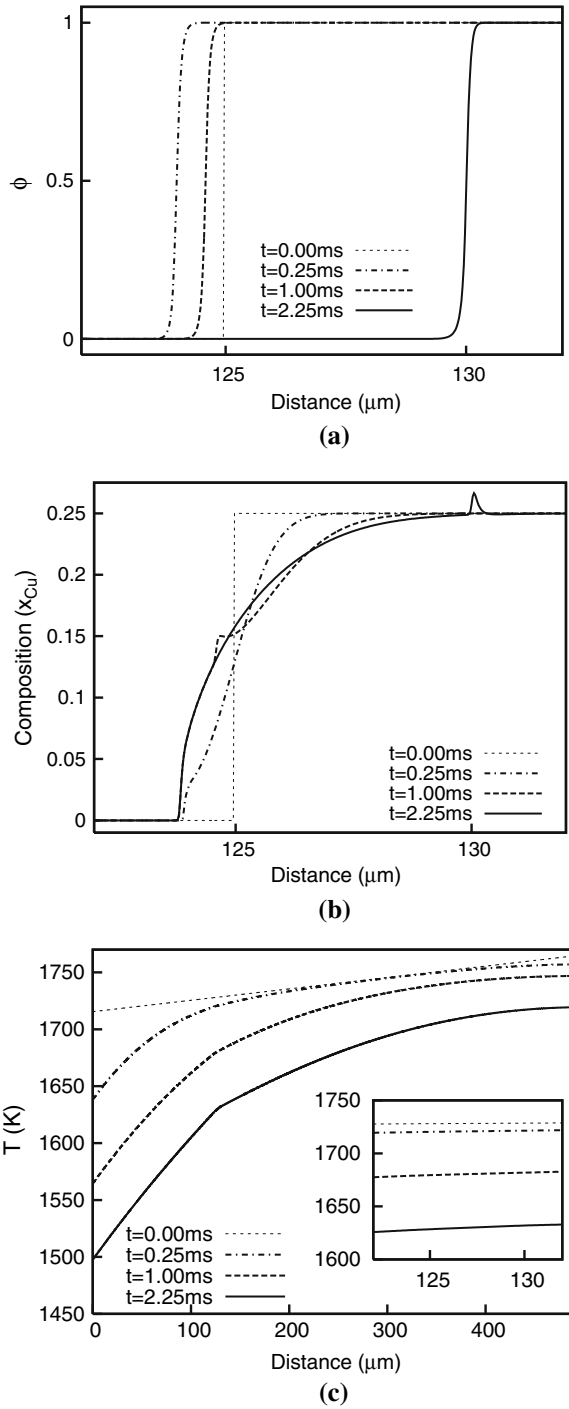

Fig. 2—Evolution of the (*a*) phase-field, (*b*) composition, and (*c*) temperature profiles near the fusion interface in the Ni side. For (a) and (b), only the active region of variation in ϕ and c is shown; the entire domain is shown in (c), with its inset showing the region covered the former two plots.

Ni-25 at. pct Cu melt, suffers a melt-back, even though heat is being extracted and the interface is below the melting point of Ni. The corresponding composition profile in Figure 2(b) shows the creation of a composition gradient ahead of the solid-liquid interface through diffusive mixing in the liquid that follows the melting of the pure base metal. The extent of the melt-back is

decided by the interaction between the imposed (negative) heat flux at the left boundary, thermal conductivity, solute diffusivity in liquid, and phase-field mobility; resolidification of the base metal starts when the decrease in liquidus temperature of the liquid due to diffusion can no longer match the fall in melt temperature through heat extraction.

As the resolidification front advances, instantaneous solid composition increases, closely following the composition gradient that had been set up during the melt-back phase. The profiles for $t = 1$ ms show an instant when the interface is almost halfway through the gradient region. The composition profile corresponding to this stage (Figure 2(b)) illustrates solute rejection at the solidifying interface, which creates a local maximum (the "blip" on the already existing gradient composition profile) ahead of the front. Finally, instantaneous solid composition reaches the far-field value c_0 when the interface crosses the gradient region (profiles at $t = 2.25$ ms). The temperature profiles in Figure 2(c) show a continuous decrease in temperature; they also show that while the local temperature gradient (G) near the left wall is fixed by the imposed heat extraction rate, G near the right wall decreases due to the insulating boundary condition. The inset of the plot corresponds to the near-interface part of the domain shown in Figures 2(a) through (b); we observe that the temperature gradient ahead of the interface is always positive, which is a characteristic of directional growth constrained by the externally imposed rate of movement of the isotherms.

To analyze the situation at the solid-liquid interface, we compute interface undercooling, which we define as $\Delta T = T_{\text{Liq}}(c_L^*) - T_{\text{int}}$, where $T_{\text{Liq}}(c_L^*)$ is the liquidus temperature corresponding to the instantaneous liquid composition at the interface, c_L^*. For the Ni-interface simulations with positive temperature gradients at the interface, the thermal undercooling term is absent,[18] and this definition of the undercooling is essentially the alloy solidification equivalent of the kinetic undercooling defined by Eq. [6]. The interface attachment coefficient μ that relates the undercooling to the front velocity is directly proportional to the phase-field mobility M_ϕ at the sharp interface limit of the phase-field model.[16] However, μ is one of the less reliably known material parameters, and the interface thickness used in estimating M_ϕ from μ is finite, subjecting the estimate of M_ϕ to errors. Hence, we have taken the M_ϕ computed from the μ^{Ni} and μ^{Cu} values given in Table I as its base value and have run simulations by varying it systematically to compute the interface undercoolings.

In Figure 3, we present two limiting cases of the undercooling *vs* time curves from simulations that use M_ϕ values differing by two orders of magnitude. We see that a higher value of M_ϕ results in a smaller steady-state undercooling; ΔT changes from ~24 to ~6 K when M_ϕ is increased 100 times from its base value. The nature of the plots, however, is very similar in two cases: there is an initial negative undercooling stage, followed by two regions where undercoolings increase at different rates, before finally reaching a steady-state value. We note that the initial negative undercooling stage corresponds to the melting of the pure substrate below its melting point; it is a case of "solutal melting" that is associated with a composition jump in systems with downward sloping liquidus lines. Rattenmayr and co-workers have analyzed[19,20] solutal melting of Al in contact with an Al-Mg alloy under isothermal condition. In contrast to those studies, here, the thermodynamic driving force for melting changes sign with time due to continuous heat extraction through the substrate.

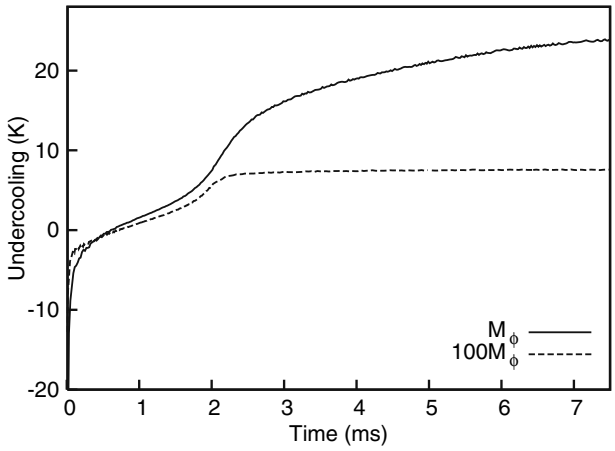

Fig. 3—Variation of interface undercooling with time in the Ni side. The dashed line corresponds to the simulation where mobility M_ϕ is increased 100 times that shown by the solid line.

We also determine the interface velocity V by extracting the interface position ($\phi = 0.5$) from the phase-field data and computing its rate of change. The variation of the interface velocity with time is shown in Figure 4 for M_ϕ values different by two orders of magnitude. The four regimes that are clearly identified in these velocity-time plots are as follows: (1) negative velocity regime in the beginning, indicating solutal melting: the rate of melting decreases continuously in this stage; (2) very small positive velocity regime: the interface starts resolidifying through the composition gradient layer; (3) transition regime: velocity increases rapidly as the

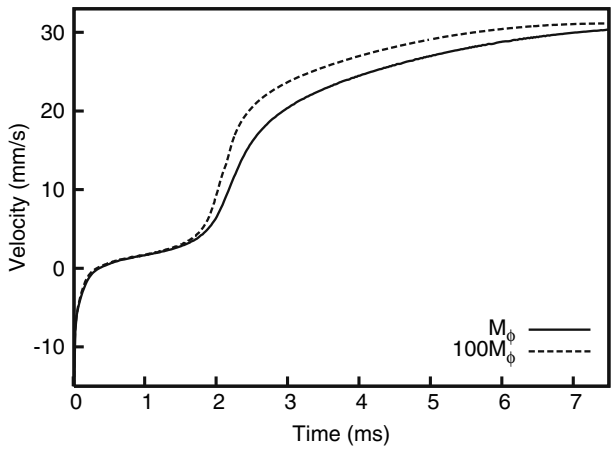

Fig. 4—Variation of interface velocity with time in the Ni side. The dashed line corresponds to the simulation where mobility M_ϕ is increased 100 times that shown by the solid line.

interface is almost toward the end of the gradient; and finally (4) steady-state regime: solidification takes place in a homogeneous liquid. This plot brings out the growth difficulty faced by the base metal due to the presence of a composition gradient during dissimilar welding. Using the time at which the transition from regime (2) to (3) takes place, t_{cr}, as a measure of the resistance to base metal growth, we plot its variation with the starting melt composition c_0 in Figure 5. This plot shows that the growth difficulty increases when the base metal is in contact with a higher concentration melt.

B. *Cu Interface*

Initial conditions for ϕ, c, and T are similar to what were used for the Ni interface; however, the liquidus line in the Cu end of the phase diagram slopes upward (that is, liquidus temperature increases with increasing Ni content of the melt), and this results in a situation that is completely different from the Ni interface. The starting composition and temperature profiles are shown in Figure 6; the position of the solid-liquid interface coincides with the jump in composition, with its temperature being at the Cu melting point (1358 K). The initial conditions, with the values chosen for G (10^5 K/m) and the melt composition c_0 (25 atom pct Ni, for which the liquidus temperature is 1466.5 K), make the entire melt ahead of the solid-liquid interface already in a deeply undercooled state and the undercooling is highest at the interface.

Under these conditions, solidification starts immediately with the composition of the solid being instantaneously adjusted to c_0; Figure 7 presents a snapshot of the events at time t = 1 ms. The temperature profile shows a distinct peak at the interface due the recalescence event in the undercooled melt; the inset of the figure also shows very clearly that the local temperature gradient in the liquid is negative, which is characteristic of unconstrained growth in undercooled melts.

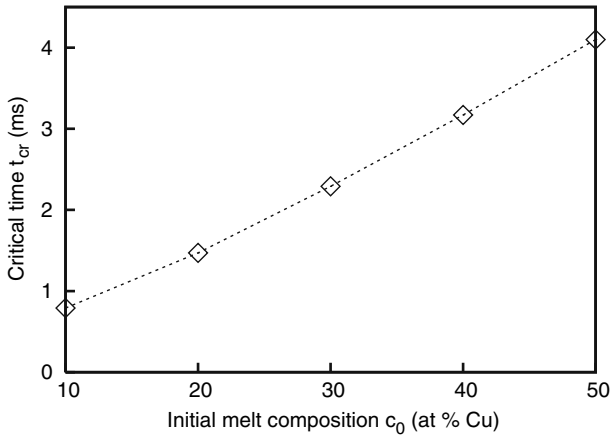

Fig. 5—Variation of the critical time t_{cr} (the transition from stage 2 to stage 3 in the velocity-time plot) with initial melt composition. The dotted line is drawn as a guide to the eye.

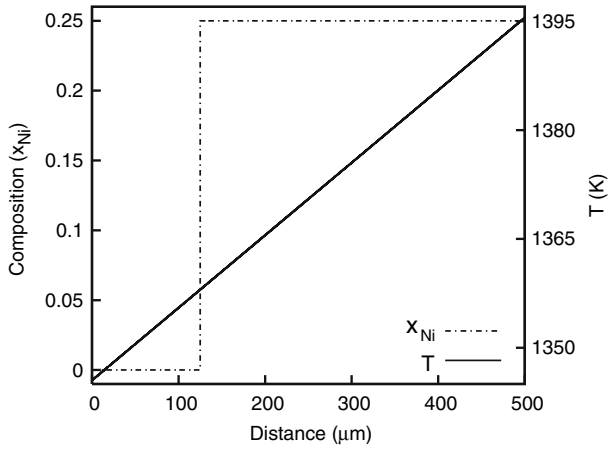

Fig. 6—Initial composition (dash-dot line) and temperature (solid line) profiles for the Cu interface simulations. The interface location coincides with the jump in composition, and the interface is at the melting temperature of pure Cu.

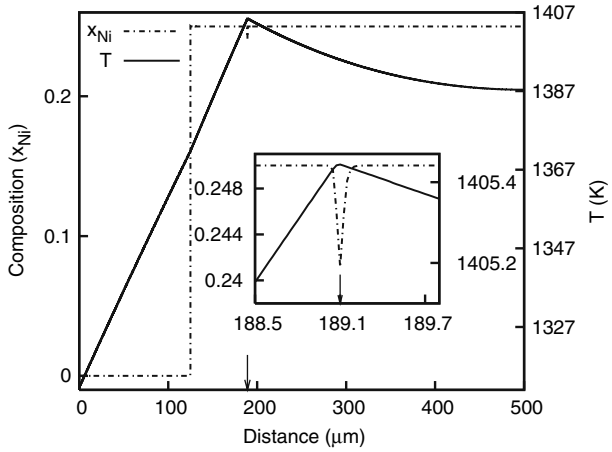

Fig. 7—Composition (dash-dot line) and temperature (solid line) profiles in the Cu side at time t = 1 ms. The inset shows the details near the interface. Arrows indicate the position of the solid-liquid interface.

We compute the interface undercooling and velocity in a fashion similar to that in the Ni interface case; we note, however, that "undercooling" in the present context is dominated by the initial bulk undercooling. The "thermal undercooling" term[18] also comes into play in the present case, because heat is removed from the interface through both the solid and the liquid (Figure 7), and this represents a case of mixed mode solidification. As Figure 8 shows, variation of both the undercooling and the velocity with time are similar, with initial very high values decreasing steadily with time. We note that these plots are drastically different from the ones for the Ni-interface simulations, highlighting the fundamental difference in the growth scenario at the two interfaces. The decrease in undercooling (and velocity) at later times in the present case reflects the influence of the insulating right wall boundary condition, which reduces the thermal undercooling and hence the driving force for the unconstrained growth.

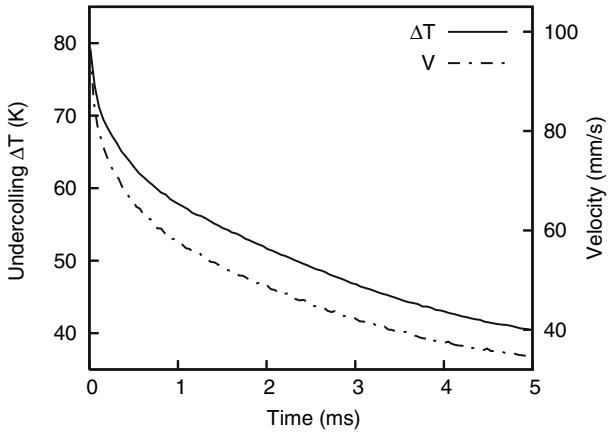

Fig. 8—Variation of interface undercooling (solid line) and velocity (dash-dot line) with time in the Cu side.

In contrast to the Ni interface, there is no driving force for solutal melting at the Cu interface as the temperature is well below the $T_{\mathrm{Liq}}(c_0)$. There exists, however, a considerable *difference* in the driving force for solidification *across* the leading and lagging parts of the diffuse solid-liquid interface region, as higher composition in the former regions implies a higher local liquidus temperature and hence a greater driving force. This asymmetry results in a completely different transformation behavior when the phase-field mobility, M_ϕ, is increased from its base value. Doing so leads to faster phase change (solidification) in the leading part of the interface, and the release of its enthalpy of fusion actually moves the interface temperature above the melting point of pure Cu, causing the lagging part of the interface to undergo a reverse transformation, namely, melting. In effect, it results in the nucleation of a solid phase with composition c_0 from the melt, thereby creating two new solid-liquid interfaces (ones involving the freshly nucleated solid) in the process.

Figures 9(a) through (c) depict the situation at $t = 0.01$ ms after the start of the simulation with mobility M_ϕ made 100 times of its base value (the results are similar for a much lower increase in M_ϕ; we have observed nucleation even at M_ϕ values 20 times the base value). The phase-field profile in Figure 9(a) shows the nucleation of a solid phase, more clearly observed in the inset, which focuses on the active transformation region. The solid Cu base metal, which was initially in the position marked "2", melts and recedes to the position "1"; the freshly nucleated solid grows from 2 toward the positive x direction to the position marked "3" (the solid-liquid interfaces will be referred to by these numbers hereafter). The composition profile in Figure 9(b) shows that the freshly nucleated solid phase has composition close to c_0 (inset); it also separates the concentrated melt from an almost pure Cu melt produced by secondary melting. The temperature profile (Figure 9(c)) exhibits a maximum at interface 3, signifying the highest rate of transformation there; it also shows the increase in local temperature beyond the melting point of Cu in regions 1 through 3, which caused melting of the substrate.

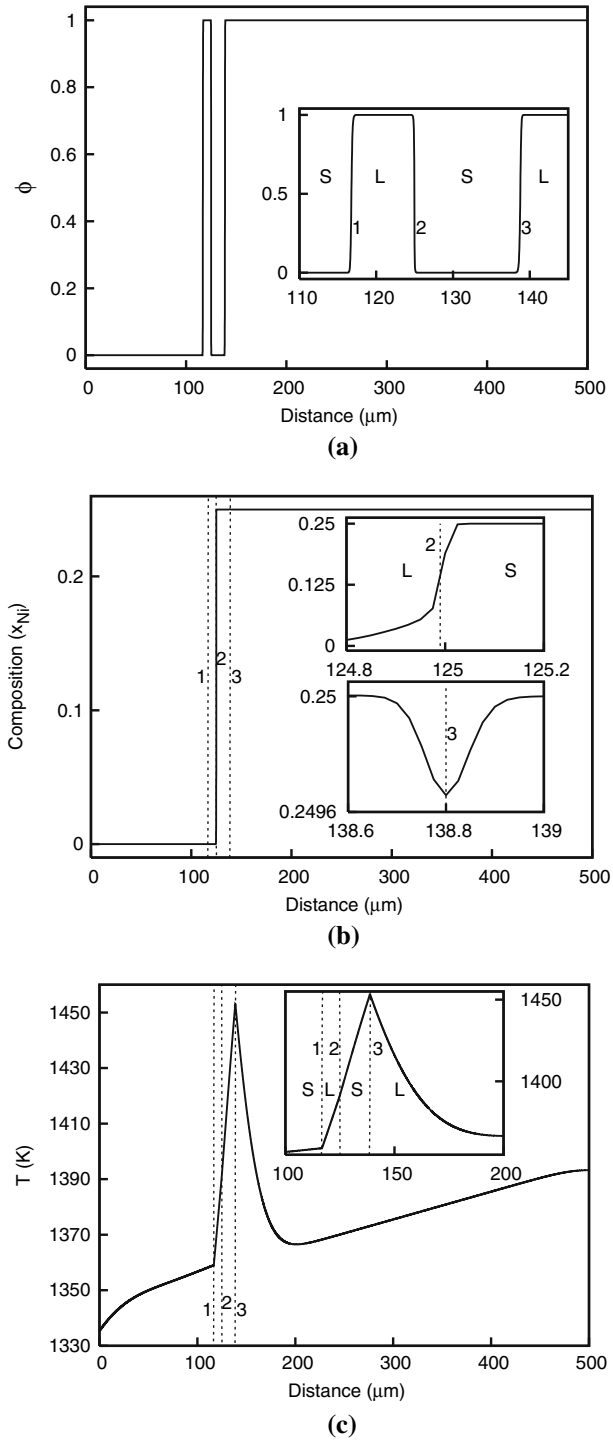

Fig. 9—Simulations in the Cu side with increased value of the mobility parameter M_ϕ: (*a*) phase-field, (*b*) composition, and (*c*) temperature profiles at $t = 0.01$ ms showing creation of three solid-liquid interfaces. Insets in (b) and (c) magnify the regions near these interfaces (the locations of which have been marked by dotted lines).

Interface 1 continues to recede as a result of the recalescence event (associated with interface 3) with decreasing velocity, while heat is extracted from the left wall; eventually, the processes balance each other, and the substrate starts to resolidify when temperature at interface 1 falls below the melting point of pure copper.

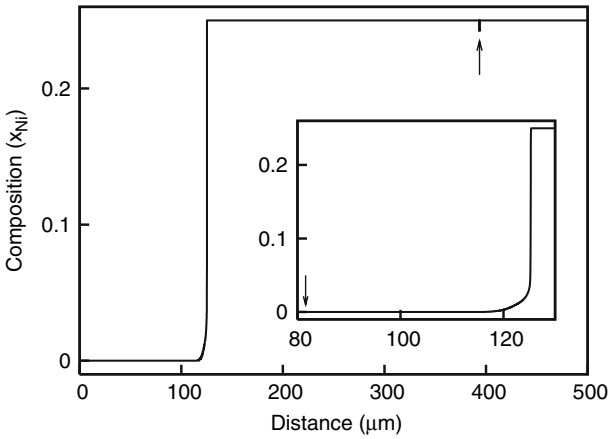

Fig. 10—Composition profile at $t = 4.5$ ms for the Cu interface simulation with increased mobility (the arrow marks the current position of the interface). The inset shows composition variation in the region affected by secondary melting, highlighting the separation between the fusion line (marked by the arrow near the left end of the inset) and the start of the alloyed region.

Ultimately, interfaces 1 and 2 merge mostly as a result of the regrowth of the substrate (interface 1). Figure 10 shows the composition profile (at $t = 4.55$ ms) after this has taken place, and the system is left with only one solid-liquid interface, which continues to advance into the remaining melt. The inset of Figure 10 shows the region until which the substrate had receded due to secondary melting; almost the entire region is pure Cu, with composition increasing steeply near the region where the initial nucleation had taken place.

The velocity history of all three interfaces (1 through 3) are presented in Figure 11; we note that both interface 1 and 3 had very high velocity initially (of melting and solidification, respectively), which decreased sharply to much lower values (and, in case of interface 1, changed sign), while interface 2 remained almost stationary. The inset of the figure zooms in on the later time span where velocities are comparatively lower; this shows the reversal of front movement for interface 1, and also a very small solidification velocity of interface 2 toward the negative x direction at later times. We also note from Figure 11 that after ~4 ms, 1 and 2 had merged, leaving 3 as the only phase transformation front.

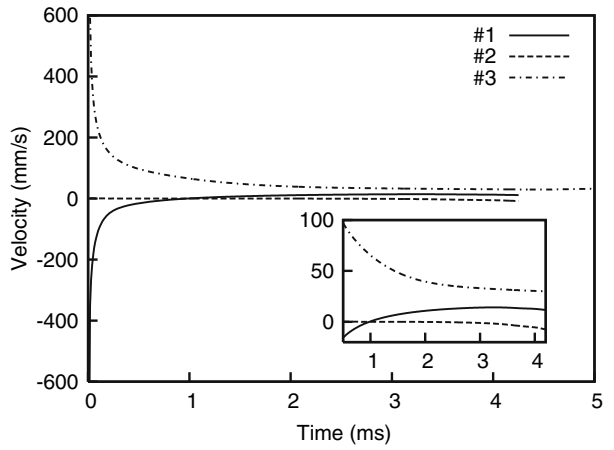

Fig. 11—Velocities of different interfaces (1 through 3) in the Cu-side simulation with increased mobility. Resolidification of the base metal leads to the annihilation of interfaces 1 and 2 after ~4 ms. The inset captures the time window where these velocities approach their steady-state limit.

IV. DISCUSSION

We have studied events at and near the fusion interfaces during solidification of dissimilar welds in the idealized setting of a pure substrate in contact with a concentrated melt, and the parameters used here corresponded to the single-phase solidification of Ni-Cu alloys. Convection in the liquid, which can have very important consequences in actual welding, is not incorporated into the model. Although the restrictive assumptions used in the model preclude any direct comparison to more complex dissimilar weld interfaces with intermetallic compound formation (as in the case of welding of Ti/Ni[11]), the simulations do provide insights that are valid not only for the welding of a Ni/Cu couple, but can also be extended to understand other dissimilar couples also. The main features of dissimilar welding revealed by the simulations are (*a*) growth difficulty of the base metal, (*b*) different modes of growth (constrained/unconstrained/mixed), and (*c*) the possibility of formation of phases with different composition at or ahead of the fusion interface. We shall now discuss the different conditions under which these can be observed, the parameters that control them, and their broader implications.

The *sign and magnitude of the liquidus* slope turn out to be the most important parameters (at least in the single-phase solidification case) for microstructure development at fusion interfaces in dissimilar welding. In the Ni side, where the liquidus slopes downward, events that take place near the interface are solutal melt-back, sluggish resolidification, and a final steady growth of the solid. We have used the time taken for the transition from the sluggish resolidification regime to a faster growth regime where composition is homogeneous, t_{cr}, to measure the magnitude of the resistance to base metal growth. This time is a significant fraction of the total time t_T for complete solidification with the steady-state velocity; for example, for the case of $c_0 = 50$ at. pct Cu, $t_{cr} \approx \frac{1}{3}\ t_T$. This translates to several tens of micrometers in terms of the microstructural length scale to which the growth is hindered.

It is also clear from the simulations that this hindrance increases with increased magnitude of the concentration gradient (Figure 5). A higher composition jump results in a steeper gradient after the initial solutal melting, and consequently to a higher slope of liquidus temperature profile in the liquid ahead of the interface, slowing the growth further. This is equivalent to a system having a steeper liquidus curve near the pure component end(s) of the phase diagram. Hence, based on our results, we expect the base metal growth to be even more difficult for systems with steep liquidus lines.

The preceding fact holds special significance for the microstructures formed near the Ti fusion interface during the laser welding of a Ti/Ni couple.[11] As the growth of β-Ti is delayed because of the unusually steep β-Ti liquidus, Ti_2Ni, the intermediate phase adjacent to the β-Ti phase field has more time to nucleate from the melt and grow toward the base metal, giving rise to a very distinct microstructure. The nucleation of monel grains on ferritic base metal reported by Nelson *et al.*[8] can be rationalized in a similar fashion; the difference in microstructure in this case with that of the Ti/Ni serves to highlight the importance of the nucleation event and the parameters that control it, namely, free energy of nucleation, interfacial energy, and preferred sites for heterogeneous nucleation. The contrast between these examples and cases where the base metal does grow into the melt (at the monel/pearlitic steel interface[8] or the Ni/melt interface in Cu/Ni[9]) illustrates the relative dominance of factors such as the magnitude of the liquidus slope, ease of nucleation of a second phase, and the kinetic parameters (conductivity, diffusivity, and interface mobility) on microstructure formation near the fusion interface.

The importance of the sign of the liquidus slope is clearly brought out by the simulations performed for the Cu interface. The drastic difference from the Ni end comes about, because the liquidus slopes positively and consequently the partition coefficient becomes greater than unity. Since liquidus temperatures are higher for increasing Ni content of the melt, the driving force for the formation of a solid solution phase is much higher than that for the growth of the pure substrate into the concentrated melt, and indeed such a phase is observed to form at the initial solid-liquid interface, either by a sudden jump in composition of the substrate or, more probably, through a ''nucleation'' event at or ahead of the interface.

Generally, nucleation is treated in phase-field models with two different approaches. One method is to hand-put critical fluctuations in the domain with probabilities satisfying classical nucleation theory.[21] In the other approach,[22] a Langevin noise term satisfying the fluctuation-dissipation theorem is added to the right-hand side of Eq. [2] and critical fluctuations emerge naturally from the simulation. Because studying nucleation was not our main aim, we did not employ either of these methods in our simulations; it took place here only as a consequence of the finite interface width interacting with the very special setup of the physical problem. In real welding situations, however, nucleation of a concentrated phase from a reasonably homogeneous melt at some distance ahead of the interface is quite feasible. In view of the large driving force available for it, nucleation can only be suppressed in regions where a very steep composition gradient exists, which was shown by the calculations of Hodaj and Desré.[23]

The initial condition of a composition jump at the interface in our simulations is based on the assumption that convection is effective in maintaining a uniform melt composition in the bulk of the weld. The results would remain qualitatively similar even if we were to start with an initial composition gradient ahead of the interface. While in practice mixing may not be fast enough to produce a step jump in composition at the initial solid-liquid interface, the interface would invariably face a concentrated melt very soon after the welding heat source (which caused the thermal melting) moves away. The initial profiles used for the present simulation idealize this situation. In summary, a positive liquidus slope is most likely to be associated with *nucleation* of the phase of different compositions from the melt, *at* or *ahead of the interface*, in place of the growth of the pure base metal into the alloy melt. We also note that the solidification mode no longer remains the usual directional growth that is used to describe convectional welding microstructures. Instead, a mixed constrained/unconstrained mode of growth may take place (Figure 7) in dissimilar welding conditions.

Nucleation of a concentrated solid solution from the melt and the consequent melt-back of the pure substrate are especially relevant to the finding of Phanikumar *et al.*[9] These investigators reported that in the Cu end of the Ni/Cu couple, there was a clear separation between the fusion line and the start of the alloyed region in the fusion zone. Our simulations show a similar separation of the almost pure Cu melt (produced by the recalescence event associated with the nucleation) from the concentrated melt by the freshly formed solid. The composition profile presented in the inset of Figure 10 shows the existence of a large unalloyed region, which had undergone melting, suggesting a mechanism for the creation of the unmixed zone observed in the experiment.[9]

The situation becomes far more complex when more than one phase can form from the melt; typical system features that would determine phase selection in those cases are the nature of liquidus curves of the phases (decides the driving force) and the interfacial energies (ease of nucleation), in addition to the kinetic factors such as thermal conductivity, diffusivity, and interface mobility. Although we do not treat multiphase solidification here, we note that for both Fe/Cu[10] and Ti/Ni[11] welds, a second phase (which nucleated from the melt near the fusion line) was observed to grow *toward* the base metal, and in both these cases, the liquidus curves of the concerned phase (Fe solid solution and Ti_2Ni, respectively) slope upward, making nucleation from the melt a very likely event.

V. CONCLUSIONS

We have presented a phase-field study of the phenomena occurring at the fusion interfaces in dissimilar welding. In particular, the simulations correspond to the welding situation of a Ni/Cu binary couple. The simulations revealed a range of new events that take place near the fusion interfaces. They also hold generic implications for other dissimilar welding conditions. The key findings of this study are summarized as follows.

1. The sign and magnitude of the liquidus curves are the two most important parameters controlling the

solidification in the Ni/Cu couple (single-phase solidification of an ideal solution).
2. For the negatively sloping liquidus at the Ni end, the presence of a composition difference at the interface severely hinders the growth of the base metal into the weldment. The magnitude of the hindrance increases with the jump in composition at the initial interface.
3. A steeper negative liquidus increases the growth difficulty.
4. A positively sloping liquidus (for example, the Cu end in Ni/Cu) is more likely to be associated with nucleation of phases from the concentrated melt. This may cause secondary melting of the base metal and create an unmixed zone between the fusion line and the alloyed weldment.
5. For the previous case, the mode of growth at the leading solidification front is a combination of directional and unconstrained growth.

ACKNOWLEDGMENT

The authors thank Dr. G. Phanikumar for useful discussions.

TABLE OF SYMBOLS

A, B	alloy constituents (Ni and Cu)
c	composition
c_L^*	liquid composition at the interface
C_p	specific heat
D_L	diffusivity in liquid
D_S	diffusivity in solid
D	phase averaged diffusivity
e	internal energy density
G	temperature gradient
g	double well potential
K	thermal conductivity
L	latent heat
M	phase-field mobility
p	interpolation function
$\dot{q}$	heat flux
S	total entropy of the system
s	entropy density
T	temperature
T_{int}	temperature at the solid-liquid interface
T_{Liq}	liquidus temperature
T_m	melting point
t	time
V	interface velocity
v_m	molar volume
W	height of the double well potential
x	spatial variable
x_i	mole fraction of constituent i
δ	interface thickness
ϵ^2	gradient entropy coefficient
μ	interface attachment coefficient
Ω	volume of the system
ϕ	phase field
σ	interfacial energy

REFERENCES

1. G. Metzger and R. Lison: *Weld. J.*, 1976, vol. 55, pp. 230s–240s.
2. Z. Sun and J.C. Ion: *J. Mater. Sci.*, 1995, vol. 30, pp. 4205–14.
3. Z. Sun and R. Karppi: *J. Mater. Proc. Technol.*, 1996, vol. 59, pp. 257–67.
4. F.K. Chung and P.S. Wei: *J. Heat Transfer*, 1999, vol. 121, pp. 451–61.
5. P.S. Wei and F.K. Chung: *Metall. Mater. Trans. B*, 2000, vol. 31B, pp. 1387–1403.
6. G. Phanikumar, P. Dutta, and K. Chattopadhyay: *Metall. Mater. Trans. B*, 2004, vol. 35B, pp. 339–50.
7. P.S. Wei, Y.K. Kuo, and J.S. Ku: *Trans. ASME J. Heat Transfer*, 2000, vol. 122, pp. 626–31.
8. T.W. Nelson, J.C. Lippold, and M.J. Mills: *Weld. J.*, 1999, vol. 78, pp. 329s–337s.
9. G. Phanikumar, P. Dutta, and K. Chattopadhyay: *Sci. Technol. Weld. Join.*, 2005, vol. 10, pp. 158–66.
10. G. Phanikumar, S. Manjini, P. Dutta, J. Mazumder, and K. Chattopadhyay: *Metall. Mater. Trans. A*, 2005, vol. 36A, pp. 2137–47.
11. S. Chatterjee, T.A. Abinandanan, and K. Chattopadhyay: *J. Mater. Sci.*, 2006, vol. 41, pp. 643–52.
12. I. Magnabosco, P. Ferro, F. Bonollo, and L. Arnberg: *Mater. Sci. Eng.*, 2006, vol. 424A, pp. 163–73.
13. W.J. Boettinger, J.A. Warren, C. Beckermann, and A. Karma: *Ann. Rev. Mater. Res.*, 2002, vol. 32, pp. 163–94.
14. O. Penrose and C. Fife: *Physica D*, 1990, vol. 43, pp. 44–62.
15. S.L. Wang, R.F. Sekerka, A.A. Wheeler, B.T. Murray, S.R. Coriell, R.J. Braun, and G.B. McFadden: *Physica D*, 1993, vol. 69, pp. 189–200.
16. J.A. Warren and W.J. Boettinger: *Acta Metall. Mater.*, 1995, vol. 43, pp. 689–703.
17. I. Loginova, G. Amberg, and J. Agren: *Acta Mater.*, 2001, vol. 49, pp. 573–81.
18. R. Trivedi and W. Kurz: *Int. Mater. Rev.*, 1994, vol. 39, pp. 49–74.
19. B. Dutta and M. Rettenmayr: *Metall. Mater. Trans. A*, 2000, vol. 31A, pp. 2713–20.
20. M. Rettenmayr, O. Warkentin, M. Rappaz, and H.E. Exner: *Acta Mater.*, 2001, vol. 49, pp. 2499–2510.
21. J.P. Simmons, C. Shen, and Y. Wang: *Scripta Mater.*, 2000, vol. 43, pp. 935–42.
22. M. Castro: *Phys. Rev. B*, 2003, vol. 67, pp. 035412-1–035412-8.
23. F. Hodaj and P.J. Desré: *Acta Mater.*, 1996, vol. 44, pp. 4485–90.